ADVANCED MATERIALS
www.advmat.de

Optical Monitoring of Water Side Permeation in Thin Film Encapsulation

*Kangling Wu, Massimo Mariello, Yves Leterrier, and Stéphanie P. Lacour**

The stability of long-term microfabricated implants is hindered by the presence of multiple water diffusion paths within artificially patterned thin-film encapsulations. Side permeation, defined as infiltration of molecules through the lateral surface of the thin structure, becomes increasingly critical with the trend of developing high-density and miniaturized neural electrodes. However, current permeability measurement methods do not account for side permeation accurately nor quantitatively. Here, a novel optical, magnesium (Mg)-based method is proposed to quantify the side water transmission rate (SWTR) through thin film encapsulation and validate the approach using micrometric polyimide (PI) and polyimide-silicon carbide (PI-SiC) multilayers. Through computed digital grayscale images collected with corroding Mg film microcells coated with the thin encapsulation, side and surface WTRs are quantified. A 4.5-fold ratio between side and surface permeation is observed, highlighting the crucial role of the PI–PI interface in lateral diffusion. Universal guidelines for the design of flexible, hermetic neural interfaces are proposed. Increasing encapsulation's width (interelectrode spacing), creating stronger interfacial interactions, and integrating high-barrier interlayers such as SiC significantly enhance the lateral hermeticity.

1. Introduction

Microfabricated, polymeric neural interfaces have become increasingly popular in neuroscience and biomedical applications due to their engineered compliance, which helps minimize the mechanical mismatch between the implants and biological tissues.[1–3] Compliance is achieved using thin (<10 µm thick) polymer substrate and superstrate (encapsulation), and embedded patterned metallic films. Despite numerous advantages, achieving long-term stability and reliable operation for such interfaces remain a challenge. The primary issue lies in the potential failure of the encapsulation layer, which can lead to leakages of body fluids and metal corrosion.[4,5] Polymers often lack sufficient resistance to water ingress, and thin-film encapsulations, e.g., ceramic single-layer or multilayer,[6,7] organic/inorganic multilayer,[8,9] are not currently hermetic enough to sustain decade long exposure in vivo.

An electrode is a usual transducer in a neural implant: it is the prime tissue-device interface and is usually wired to an embedded metallic interconnect.[10–12] Its design requires the encapsulation film to host an opening enabling tissue-electrode charge transfer. This results in multiple diffusion paths for water molecules: perpendicularly through the surface (surface permeation) and laterally through the exposed sidewalls and interfaces (side permeation) (**Figure 1**). The water transmission rate (WTR) usually refers to the surface permeation process and helps define the barrier performance of encapsulation films. With increasing number of electrodes and minimal dimensions,[13–15] side permeation through the lateral portion of the encapsulation film should be monitored. The optical calcium (Ca) test enabled to evaluate the lateral water permeation in organic light-emitting diode (OLED) encapsulations,[16–18] but its extreme moisture-sensitivity makes it incompatible with in vivo experiments. Mg films are a promising alternative, due to their sensitivity to water, visibility during the corrosion process, and compatibility with the process flow of minimized devices; so far only qualitative observations[6,9] of surface permeation have been reported.[19]

In this work, we report an optical Mg film method to quantitatively assess the water side permeation in thin-film encapsulation for implantable devices. In a first step, the nonuniform corrosion of Mg exposed to water molecules is carefully analyzed using grayscale image processing and energy-dispersive X-ray spectroscopy (EDX) acquired in scanning electron microscope. In a second step, we quantify the surface and side WTRs and lag time of water diffusion through PI under accelerated

K. Wu, M. Mariello, S. P. Lacour
Laboratory for Soft Bioelectronic Interfaces (LSBI)
Neuro-X Institute
École Polytechnique Fédérale de Lausanne (EPFL)
Geneva CH-1202, Switzerland
E-mail: stephanie.lacour@epfl.ch

M. Mariello, Y. Leterrier
Laboratory for Processing of Advanced Composites (LPAC)
Institute of Materials, École Polytechnique Fédérale de Lausanne (EPFL)
Lausanne CH-1015, Switzerland

M. Mariello
Institute of Biomedical Engineering (IBME)
Department of Engineering Science
University of Oxford
Oxford OX3 7DQ, UK

The ORCID identification number(s) for the author(s) of this article can be found under https://doi.org/10.1002/adma.202310201

DOI: 10.1002/adma.202310201

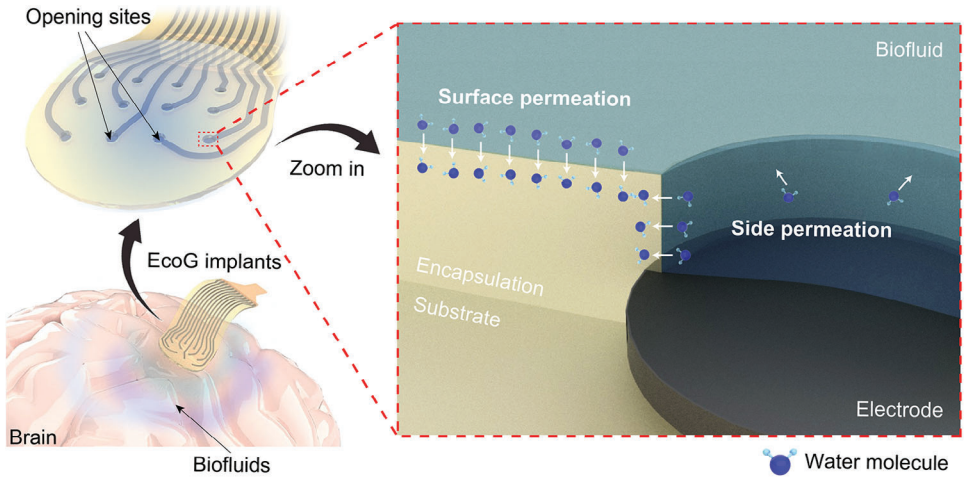

Figure 1. Multiple diffusion paths through a microfabricated electrode implant. Side permeation targets the walls of the patterned encapsulation film.

physiological conditions (saline solution, 57 °C) using grayscale images of Mg disks for various encapsulations geometries. In a third step, we investigate the influence of an additional conformable SiC interlayer on the permeation mechanisms. Finally, we assess the benefit of the PI-SiC multilayer to protect an electrocorticogram (ECoG) device against water side permeation.

2. Results and Discussion

2.1. Optical Mg Microcells and Grayscale Image Processing

Mg reacts with water and produces magnesium hydroxide ($Mg(OH)_2$), according to the following chemical reaction

$$Mg + 2H_2O \rightarrow Mg(OH)_2 + H_2 \quad (1)$$

During corrosion, Mg visually switches from bright to dark gray,[20] as a sign of water ingress. We design a microcell, in which a Mg disk (300 nm thickness, 0.5 mm radius) is laminated between 2 layers of 1 µm thick PI to mimic side permeation in standard PI-based flexible electrodes. 20 nm thick titanium (Ti) thin films are sputtered on the PI and the Mg to promote the PI-Mg adhesion and protect Mg from O_2 plasma etching. The distance between the edges of the Mg disk and PI disk, named as width of encapsulation, is varied between 20 and 150 µm. A 400 nm thick SiC layer is deposited using plasma-enhanced chemical vapor deposition (PECVD) on the top of PI to suppress the surface diffusion in favor of the edge diffusion (Figure S1, Supporting Information). An array of 144 microcells with a range of geometries are produced on a flat, transparent glass wafer for constant and stable optical observation during monthly soaking in a 57 °C phosphate-buffered saline (PBS) solution. The PBS solution is replenished every week. Here, we elevate the temperature to 57 °C to accelerate the aging. The glass wafer is inverted onto a black polymethyl methacrylate (PMMA) substrate to eliminate the shadow effect of the top SiC layer (Figure S2, Supporting Information), then placed on a motorized stage with a resolution of 1 µm for automated positioning and capturing Mg images on a Leica DVM6 microscope in reflection mode. During the image capture process, the light emanating from the microscope's lens travels through the glass wafer and the bottom PI layer before getting reflected off the Mg film, ultimately returning to the microscope's lens. The resulting digital images (1600 × 1200 pixels) with each pixel of 1.096 µm^2 surface area are recorded on a computer for further processing (**Figure 2a**).

256-level grayscale images of the individual microcells are captured to quantify the degradation of the encapsulated Mg disks. It turns out that the corrosion of Mg exposed to water vapor is nonuniform, as revealed under scanning electron microscopy (SEM) (Figure 2b) with EDX analysis of Mg and oxygen (O) elements (Figure 2c). We build the function of corrosion level and Mg brightness by analyzing the proportion of O/Mg of pixels with different grayscales. First, the nonuniformly corroded Mg disk is imaged. The resulting RGB photo is then transformed into a grayscale image. This conversion involves determining the grayscale value (GV) using the red (R), green (G), and blue (B) color weights, following the luminosity method[21]

$$GV = 0.2989 \cdot R + 0.5817 \cdot G + 0.1140 \cdot B \quad (2)$$

The grayscale value (GV) is affected by the exposure time of the Leica microscope. When the exposure time is not within a proper range, either the dark Mg becomes invisible for observation (less than 8 ms) or the image of pristine Mg is overexposed (more than 20.5 ms) (Figure S4, Supporting Information). In this study, we opt for an exposure time of 15.5 ms for optical observation.

Subsequently, cross sections of the microcells are prepared at different positions and for various exposure durations by focused ion beam (FIB) to reveal the progress of the corrosion of the Mg film. The cross sections are examined using SEM and an EDX line scan analysis is used to obtain the O/Mg atomic ratios. The O/Mg spectrums of partially and wholly corroded Mg are vastly distinguishable, indicating that the resolution of EDX analysis is sufficient to identify different corrosion portions (Figure 2d). Finally, we map the FIB cuttings in the mirrored optical image to determine the grayscale values of pixels corresponding to the EDX signals (Figure S3, Supporting Information). From the results, we find that between the pristine Mg (GV ≥ 160, corrosion level = 0) and the final product $Mg(OH)_2$ (GV < 40, corrosion level = 1), the Mg partial corrosion level linearly decreases

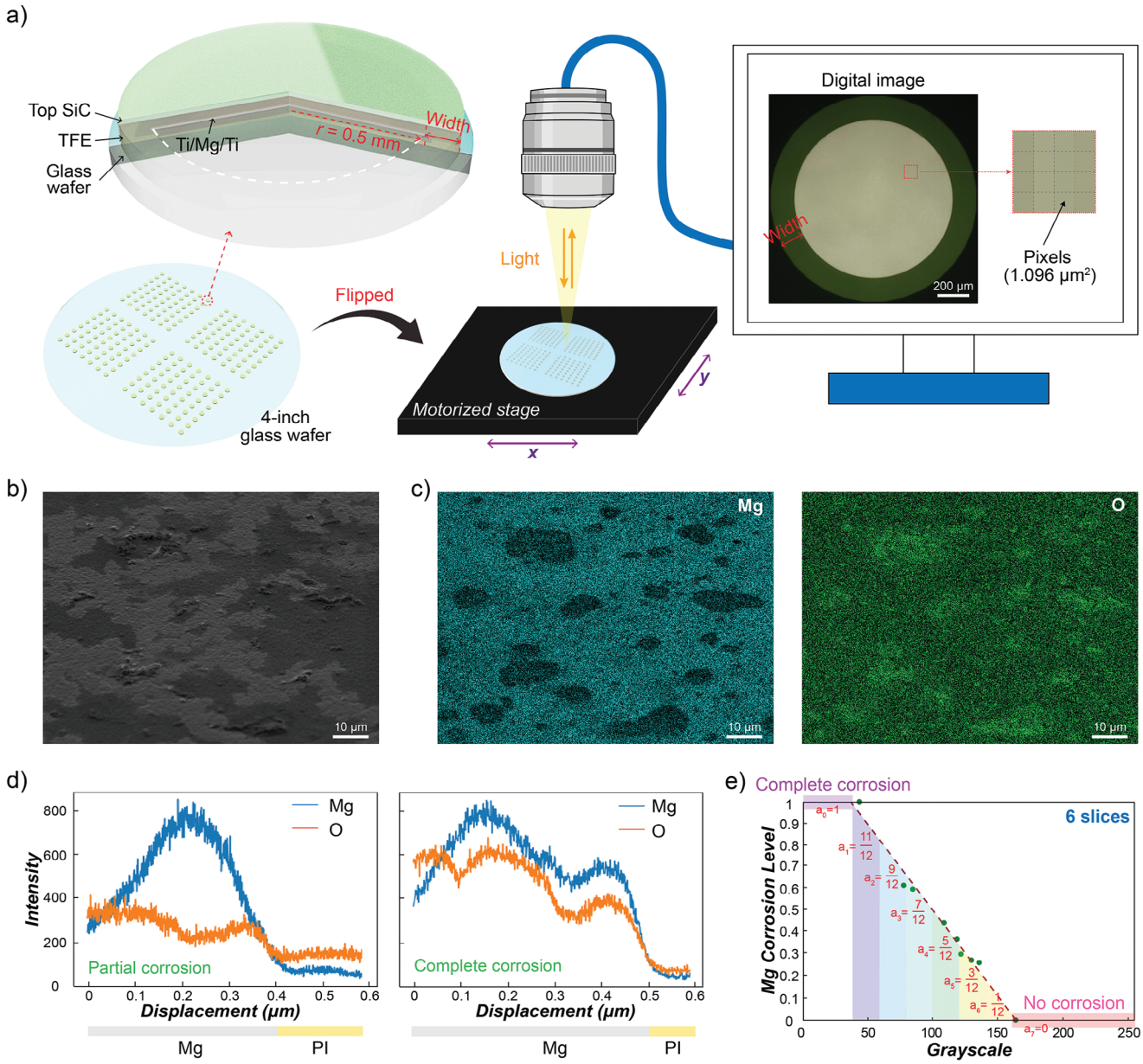

Figure 2. a) Experimental setup of optical Mg test; the thin film encapsulation (TFE) may be PI or PI/SiC. b) SEM image and c) EDX map scans (Mg Kα 1, 2 and O Kα 1) of corroded Mg directly exposed to water vapor at 57 °C for 1 day. d) Through-thickness EDX line scan results for partially and wholly corroded Mg. e) The function of Mg corrosion levels and grayscale values.

with the grayscale value (Figure 2e). When the exposure time of the digital microscope varies from 10.5 to 20.5 ms, the linear decrease of corrosion portion on grayscale still exists, while the varied slopes is related to the different increase rate of grayscale of raw and corroded Mg to exposure time (Figure S4, Supporting Information). Thus, even though various encapsulation layers or parameters will influence the Mg color, the function between Mg corrosion level and optical color can be quickly decided after detecting the grayscale values of images of raw and corroded Mg disks.

The normalized Mg corrosion area (NMgCA) of individual microcells is calculated by counting the pixel numbers in grayscale groups corresponding to different corrosion levels and then normalized by the total pixel numbers, depending on the linear relationship between corrosion lever and grayscale (Figure 2e)

$$NMgCA = \frac{1}{N}\left(\sum_{i=0}^{n} a_i N_i\right) \tag{3}$$

Here, N is the sum of pixel numbers, $a_0 = 1$ is the corrosion coefficient of group 0 (fully corroded, GV < 40), and $a_i = (2n - 2i + 1)/2n$ when $i > 0$ is the corrosion coefficient of group i, N_i

is the number of pixels in group i and n is the number of slices between GV 40 and 160. We choose $n = 6$ as the trade-off of computation and accuracy as the calculated results converge when $n \geq 6$ (Figure S5, Supporting Information).

As per the standard interpretation of water transmission rate $WTR = \Delta m_{H_2O}/(A_{en} \cdot \Delta t)$, $A_{en}$is the surface area of encapsulation crossed by the water molecules flux, $\Delta m_{H_2O}/\Delta t$ is the temporal variation of water mass at the steady state, the SWTR is calculated as follows when the surface permeation is blocked

$$SWTR = \frac{1}{A_d} \cdot \frac{\Delta m_{H_2O}}{\Delta t} \tag{4}$$

where $A_d = \pi \phi_{out} h_{en}$ is the sidewall area, ϕ_{out} is the outer diameter of the encapsulation, and h_{en} is the thickness of encapsulation (Figure S6, Supporting Information).

We can show that the SWTR is proportional to the growth rate of the NMgCA at the steady state

$$SWTR = 2 \cdot \rho_{Mg} \cdot h_{Mg} \cdot \frac{A_{Mg}}{A_d} \cdot \frac{M_{H_2O}}{M_{Mg}} \cdot k \tag{5}$$

where $\rho_{Mg} = 1.738$ g cm^{-3} is the mass density of Mg, $h_{Mg} = 300$ nm is the thickness of Mg, $A_{Mg} = \pi r_{Mg}^2 = \pi \cdot 500^2$ μm^2 is the surface area of Mg disk, $M_{H_2O} = 18.016$ and $M_{Mg} = 24.305$ g mol^{-1} are the molar masses of water and Mg, $A_d = 2\pi(1000 + 2 \cdot w)$ μm^2 varies with the width of encapsulation w, k is the slope of NMgCA to time at steady state. The full derivation of (Equation (5)) is reported in the Supporting Information. The intercept at x axis (time intercept) is named as the lag time (Figure S7, Supporting Information).

2.2. Implementation to Quantification of Surface Permeation

We assess the feasibility of the optical Mg method for quantifying water surface permeation. Different from the side permeation setup, a 20 μm thick PI layer is coated on the 0.5 mm radius Mg/Ti disks for surface permeation study. A 1 μm thick PI layer is added between metallic films and glass substrate to avoid delamination during the soaking test. The Ti layer on top of Mg is removed as it significantly reduces water permeation (Figure S8, Supporting Information) and no surface treatment is applied on the bottom PI substrate. We monitor the Mg corrosion through the glass side with the same Leica microscope every hour during 57 °C PBS soaking. The optical images reveal that water surface permeation occurs along the thickness direction, evident in the gradual darkening of the entire Mg microcells over time (**Figure 3a**). After the first 5 h of soaking, the NMgCA slightly increases, as the sign of water at the Mg surface starts to initiate corrosion. Then, the NMgCA value linearly increases with the soaking time, indicating a steady state diffusion. Finally, it reaches a saturation state, with a plateau on the curve. As mentioned before, we only use the steady-state NMgCA change rate to calculate the WTR (Figure 3b), which is

$$WTR = 2 \cdot \rho_{Mg} \cdot h_{Mg} \cdot \frac{A_{Mg}}{A_{en}} \cdot \frac{M_{H_2O}}{M_{Mg}} \cdot k \tag{6}$$

Here, the surface area of encapsulation A_{en} is equal to the surface area of Mg disk A_{Mg}. For the 20 μm thick PI at 57 °C the calculation gives $WTR = 0.83$ g m^{-2} day^{-1} and lag time $t_{lag} = 0.155$ day.

However, the corrosion product $Mg(OH)_2$ also acts as a barrier, which should be considered to calculate the water transmission rate of the PI layer. The grayscale values represent varying levels of corrosion, in other word, varying thickness of $Mg(OH)_2$. The WTR values at each corrosion area are decided by the 20 μm PI and the $Mg(OH)_2$ at this corrosion level. The water mass change rate at the steady state can be calculated as the sum of water diffusing rate through different corrosion regions, which should be equal to the WTR value calculated by NMgCA multiplied by the surface area of encapsulation. More detailed derivation is written in the Supporting Information

$$\frac{\Delta m_{H_2O}}{\Delta t} = \sum_{i=0}^{7} WTR_i A_i = WTR \times A_{en} \tag{7}$$

We find that the WTR of full-corrosion $Mg(OH)_2$ is equal to 1.46 g m^{-2} day^{-1} and that of the 20 μm PI is equal to 8.53 g m^{-2} day^{-1} at 57 °C in PBS solution. The WTR-calculating data perfectly fit the raw data until the end of steady state (Figure 3c). The corresponding permeability of the 20 μm thick PI, defined as the WTR multiplied by the thickness is 0.17 g mm m^{-2} day^{-1} (57 °C, in PBS solution). This value is close to values reported in the literature[22,23] and to the value measured by a standard permeation cell (Table S1, Supporting Information). Even after correcting for the presence of $Mg(OH)_2$, the WTR for the 20 μm PI layer is 10.28 times larger than the value directly calculated from the slope, representing the equivalent WTR of the bilayer consisting of PI and $Mg(OH)_2$, the lag time values from 2 methods are quite similar (Figure 3d).

2.3. Implementation to Quantification of Side Permeation

Next, we measure the water side permeation through different encapsulation widths. The PI bilayer and top SiC are patterned to several widths: 20, 50, 100, and 150 μm and then immersed into 57 °C saline solution. Here, no surface treatment is applied on the bottom PI substrate as for surface permeation study. Unlike Mg corrosion induced by surface permeation, the optical bright-to-dark transformation of the Mg disks starts from the edge and then gradually attaches to the center of the disk, similarly for each investigated width. This implies that only lateral diffusion occurred, and the top SiC coating suppressed the surface diffusion (Figure 3e). Even though SiC films are not perfectly pinhole-free, the pinhole-induced Mg failures are easily read from the pictures (Figure S9, Supporting Information) and excluded from the data analysis. We assume the protective efficiency of $Mg(OH)_2$ against water side permeation is negligible as the hollow structure of $Mg(OH)_2$ is detected from its cross-section SEM image (Figure S10, Supporting Information). Therefore, the SWTR is calculated from the slope of NMgCA to time, as described in Equation (5).

It is evident that increasing the width of the encapsulation significantly delays and reduces the lateral permeation in the no-surface-treatment PI bilayer, both visually (Figure 3e) and quantitatively (Figure 3f). The SWTR value decreases from 38.99 ± 1.26

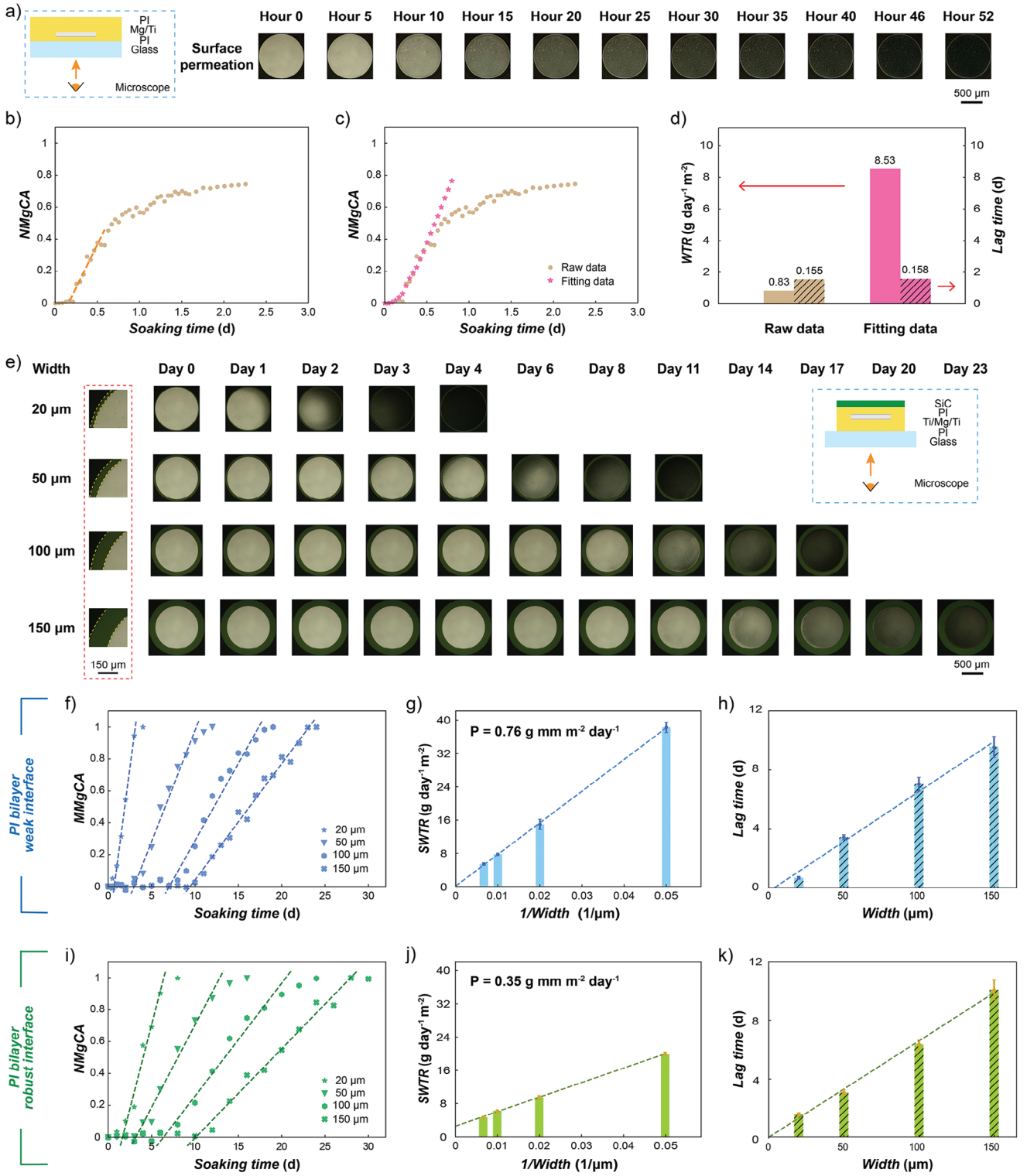

Figure 3. a) Schematic cross-section of the experimental set-up and top view, optical images of Mg disks corrosion due to surface permeation over time. b) NMgCA varies with the soaking time for surface permeation, $n = 144$. c) The curves of raw and fitted NMgCA data vary with soaking time. d) Raw and fitted WTR and lag time. e) Schematic cross-section of a Mg disk embedded within a thin film encapsulation disk leaving a ring of TFE around the Mg disk. Optical images of corroding Mg disks protected by rings of increasing widths. f) NMgCA varies with the soaking time for the weak-interface PI bilayer with different widths, $n \geq 10$. g) SWTR value linearly increases with the width of weak-interface PI bilayer, $n \geq 10$. h) Lag time linearly increases with the width of weak-interface PI bilayer, $n \geq 10$. i) NMgCAs vary with the soaking time for the robust-interface PI bilayer with different widths, $n \geq 10$. j) SWTR linearly increases with the width of robust-interface PI bilayer, $n \geq 10$. k) Lag time linearly increases with the width of robust-interface PI bilayer, $n \geq 10$.

to 6.19 ± 0.35 g m^{-2} day^{-1} (Figure 3g), and the lag time increases from 0.70 ± 0.10 to 9.53 ± 0.72 day (Figure 3h) when the barrier width increases from 20 to 150 µm. The results suggest that, even for the nontreated PI–PI interface, water side permeation could be delayed to over 1 year at 37 °C when the width of encapsulation reaches 1.5 mm. We also observe that the SWTR scales with the inverse width, which is consistent with a constant permeability value, equal to 0.76 g mm m^{-2} day^{-1} from the product of SWTR and diffusion distance (Figure 3g). Compared to the surface permeation, the side permeability is around 4.5 times larger, indicating that the interface between the two PI layers plays a significant role in lateral permeation. For the same dimension of PI layer (20 µm), the lag time of surface permeation (0.158 day) is lower than that for side permeation (0.70 day). This is due to a more prompt accumulation of water molecules from the very large surface area, in contrast to the much lower side area to hit a critical water amount initiating the Mg corrosion.[20] The simulated time profiles of water diffusion through 20 µm thick or 20 µm wide PI further support our assumption (Figure S11, Supporting Information).

2.4. Influence of Interface Adhesion on Side Permeation

Next, we evaluate the impact of the interface on side permeation using O_2 plasma treatment and two PI films (substrate and superstrate). Upon exposure to O_2 plasma, the PI surface roughens oxidizing carbon bonds[24,25] to form a solid and robust PI–PI interface with an adhesion energy of 320 J m^{-2}. In contrast, the adhesion energy of the unmodified interface is only 10 J m^{-2} (Figure S12, Supporting Information). Compared to the untreated PI bilayer, the activated interface restrains the side permeation as reflected by the reduced Mg degradation rate (Figure 3i), resulting in smaller SWTR values at each encapsulation width (Figure 3j). A constant permeability of 0.35 g mm m^{-2} day^{-1} is obtained for the robust-interface PI bilayer, a value that is more than two times lower compared with the untreated interface case. No significant change of lag time is noticed between weak-interface or robust-interface PI encapsulations (Figure 3k). This is because the interface area is negligible to the sidewall area, barely affecting the time profiles of water accumulation (Figure S13, Supporting Information). Comparing to surface permeation, the permeability of the robust interface PI bilayer is still twice larger, implying that the patterning steps may induce extra defects in the encapsulation sidewalls or interfaces.

2.5. Influence of SiC Interlayers on Side Permeation

Next, we introduce SiC interlayers into the system to enhance the overall lateral hermeticity.[26,27] The high-barrier performance of PECVD SiC against water surface permeation has been confirmed (Figure S1, Supporting Information). In this context, our focus shifts to investigating the water side permeation behavior through PI-SiC stacks. The Mg disks are sandwiched between two layers of PECVD SiC, each with a thickness of 130 nm; a thinner SiC film also covers the wall of the Mg disks. The remaining structure of the stacks follows the same design as that of the PI-Mg samples. We proceed to pattern the encapsulation layer widths to 20, 50, 100, and 150 µm, followed by immersing the wafer in a 57 °C PBS solution. We evaluate the Mg corrosion over time. Despite the SiC interlayer causing a slight darkening of the Mg color, determining the corrosion level based on grayscale remains feasible due to the persisting linear relationship between these two parameters (Figure S4, Supporting Information).

No visible corrosion was detected from the optical images after 10 days of soaking in PBS, for four different encapsulation widths. The oxidation process eventually progresses and is complete after 100 days of immersion for a 150 µm width (**Figure 4a**). Corrosion of Mg initiates from the edges but in contrast to the PI-Mg disks, the corrosion pattern of Mg is more uniform along the diffusion front. This consistent corrosion behavior is attributed to the presence of impermeable SiC layers, restricting water diffusion solely along the SiC-SiC interface. We deduce the SWTR and lag time for the SiC–SiC interface by analyzing the slope of the NMgCA against soaking time during the steady state (Figure 4b). Given the challenge of precisely defining the interface thickness, we opt to use the combined thickness of PI and SiC (2.26 µm) to calculate the equivalent sidewall area. We have observed a distinct mechanism of water-side permeation at the SiC–SiC interface: the permeability is not constant, but rather decreases as the inverse width increases, in other word, as the width decreases (Figure 4c). The lag time associated with water diffusion through the PI-SiC stacks still adheres to a linear increment with respect to the width and the y-intercept of the linear fit line is 20.86 days (Figure 4d). This suggests that even at extreme dimensions, the SiC layer effectively shields sensitive components against water side permeation, in agreement to our COMSOL stimulation results (Figure S14, Supporting Information). For high-density electrodes or geometrically engineered stretchable interconnects with an extremely narrow width of encapsulation, integrating SiC interlayers into the encapsulation stack is a favorable choice to block water side permeation.

2.6. In Vivo Implementation

We finally assess the barrier performance of the PI-SiC stacks to side permeation in microfabricated electrode arrays prepared for electrocorticography (ECoG), as the presence of laterally diffused water can lead to variation of the electrochemical impedance of the electrodes and impact the quality of recordings. The thickness of barrier layers for PI-ECoG and PI-SiC-ECoG devices are the same as the Mg samples, while the metal is formed as a Ti/Pt/Ti (20/100/20 nm) multilayer. The SiC coating is also deposited on top of the PI layer to prevent surface permeation in both the PI-ECoG and PI-SiC-ECoG. The surface treatment includes O_2 plasma (200 W, 30 s) and an adhesion promoter (VM652) for PI-ECoG samples as the tradeoff of adhesion between PI–PI and PI–Ti (Figure S15, Supporting Information). The diameter of the exposed metallic electrodes is defined as 120 µm, with a 20 µm offset between the metal edge and the opening site. Additionally, the spacing between electrodes is maintained at 1.15 mm, measured from center to center (Figure S16, Supporting Information). We estimate the electrochemical stability of ECoG electrodes encapsulated by PI bilayer and PI-SiC multilayers during accelerated aging at 57 °C in PBS solution by electrochemical impedance spectroscopy (EIS). The EIS spectra of both types of

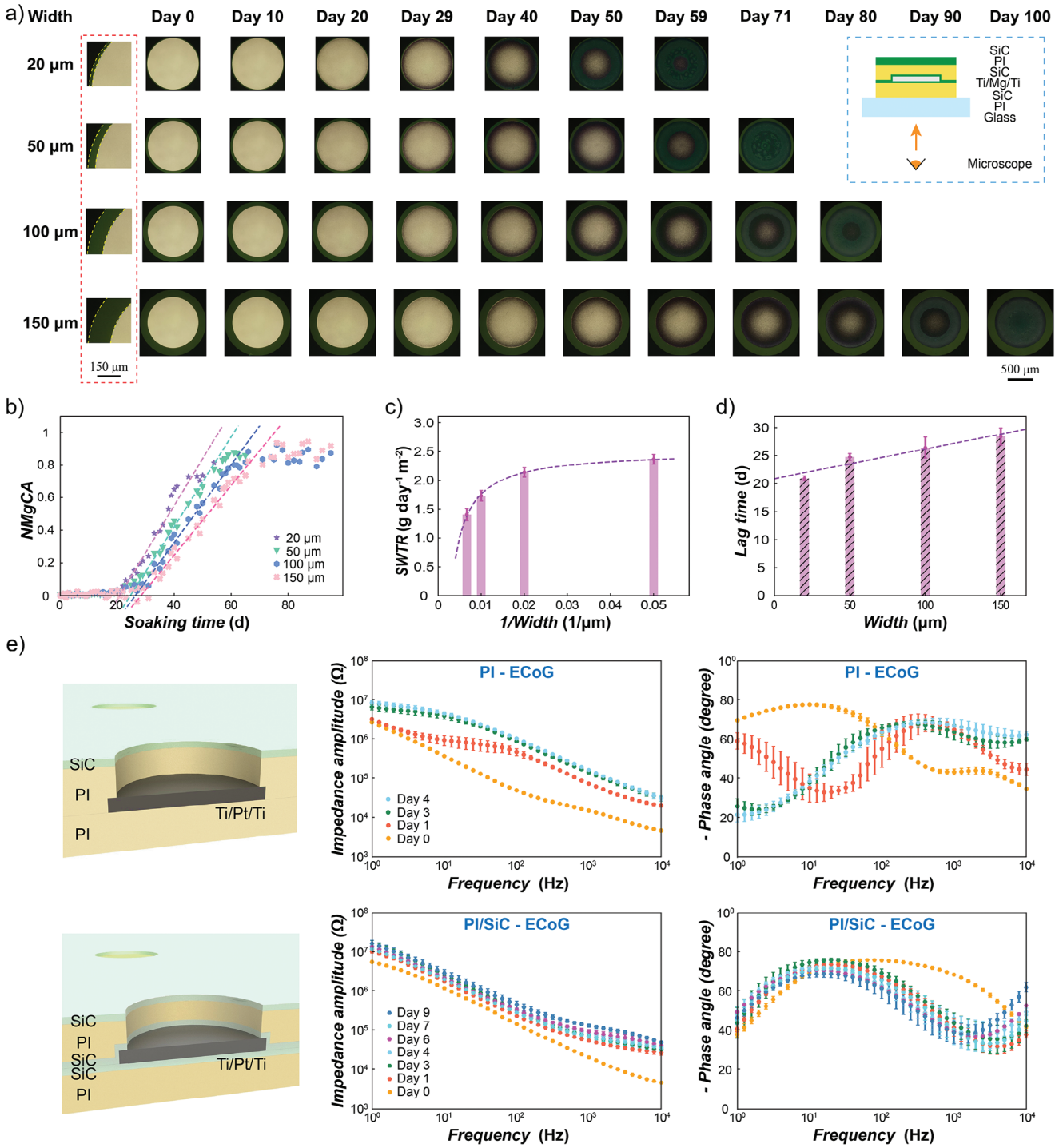

Figure 4. a) Side view schematic and optical images of Mg disks protected by different widths of PI-SiC multilayer during the soaking. b) NMgCAs vary with the soaking time for the PI-SiC encapsulation with different widths, $n \geq 10$. c) SWTR increases with the inverse width of PI-SiC multilayer, $n \geq 10$. d) Lag time linearly increases with the width of PI-SiC multilayer, $n \geq 10$. e) EIS results of PI-ECoG and PI-SiC-ECoG, $n = 9$.

electrodes demonstrate that the impermeable SiC interlayers significantly reduce water lateral permeation: the impedance amplitude (at 1 kHZ) of PI-ECoG increases from 14.7 (day 0) to 157.2 kΩ (day 4), and the phase rises from 43.43° to 66.96°, while the impedance and phase plots of PI-SiC-ECoG are nearly constant even after 9 days of soaking (Figure 4d). The trend aligns consistently with the optical observations: side permeation in the PI film occurs within the initial 0.5 days of soaking in a 57 °C PBS solution, whereas in the PI-SiC stack, the lateral permeation is delayed up to 10 days.

3. Conclusions

In conclusion, the proposed optical Mg test is a promising method for evaluating unprecedently water sideway diffusion in thin-film encapsulation. The nonuniform Mg corrosion limits the usage of binary images for further analysis. Nevertheless, digital grayscale optical micrographs enable to accurately quantify the surface and side water transmission rate, through a linear correlation between corrosion level and Mg grayscale value revealed by EDX analysis. The surface permeability of 0.17 g mm m^{-2} day^{-1} and side permeability of 0.76 g mm m^{-2} day^{-1} are measured separately for PI thin-film at 57 °C in PBS solution, the difference being attributed to the permeation of water molecules along the PI–PI interface. After an oxygen plasma treatment on PI–PI interface, the side permeability of PI is reduced to 0.35 g mm m^{-2} day^{-1}. For PI-based devices with electrode patterns, the side permeation is likely to dominate encapsulation failure when the ratio of surface area to thickness is less than 4.5 (for weak PI–PI interface) or 2 (for robust PI–PI interface) times of the sidewall area divided by width. Introducing high-barrier inorganic interlayers can significantly decrease or slow down side permeation: SWTR is reduced from 38.99 (PI) to 2.41 (PI-SiC) g mm m^{-2} day^{-1} and lag time is extended from 0.7 (PI) to 20.8 (PI-SiC) days at 20 µm width. Even when the width of the SiC interlayer is reduced to an extremely small dimension (e.g., 130 nm), significant lateral hermeticity is likely to be achieved in PI-SiC system due to the observed trend of decreasing permeability with decreasing width. The stable electrochemical impedance observed over a 9-day period of soaking in 57 °C PBS for the 9 electrodes in the ECoG devices serves as validation for the adequate protection provided by the PI-SiC multilayer. The broad width of encapsulation, strong and robust interfaces and high-barrier inorganic that conformably covers the sidewalls of sensitive components are desired for designing hermetic neural interfaces. The optical Mg method is applicable for quantifying water side permeation in various thin-film barriers that are transparent to visible light, such as PI, Parylene C, PDMS, PET, Al_2O_3, TiO_2, etc. However, barriers with opaqueness pose limitations to this method, and in such cases, the electrical Mg test can be employed to overcome this constraint.

4. Experimental Section

Microfabrication of PI-Mg-PI Disks for Side Permeation: The fabrication started with the pretreatment of 4 in. glass wafer. A glass wafer was cleaned with acetone and isopropyl alcohol (IPA) and activated by 600 W O_2 Plasma (PINK GmbH Thermosysteme, V10-G) for 10 min, then adhesion promoter (VM652, 1 vl% VM651 diluted in IPA, HD MicroSystems) was spin-coated and dried at room temperature. Then 1 µm PI (HD Microsystems GmbH, catalog no. PI2610) was spin-coated on the pretreated glass wafer. 20 nm thick Ti layers were sputtered (AC450, Alliance-Concept) between PI and Mg as the adhesion layer. 300 nm thick Mg was thermally evaporated (E300, Alliance-Concept) as the humidity sensor. The 0.5 mm radius disks were patterned by the lift-off (10 mins 80 kHz/100% power ultrasonic bath in acetone). The other 1 µm PI layer was coated on top with/without O_2 plasma (PINK, 200 W/2 min) pretreatment for robust PI–PI interface or weak interface. Then, a 400 nm thick PECVD SiC was deposited by Oxford PlasmaLab system 100 PECVD (133 sccm Ar, 60 sccm CH_4, and 375 sccm 2% SiH_4/Ar, 25 W, 300 °C, 30 min of deposition). The final etching step (Corial 210IL ICP-RIE etch system) patterned the stacks to 4 widths: 20, 50, 100, and 150 µm.

Microfabrication of PI-Mg-PI Disks for Surface Permeation: The same pretreatment was adapted to form the strong adhesion between the bottom 1 µm PI layer and the glass wafer, followed by the lift-off of patterning Ti/Mg films. No top Ti was sputtered on the Mg films. Then, a 20 µm PI layer was coated on the top, achieved by 2 times of spin-coating and soft bake of 10 µm thick PI layers with a 2 min 200 W O_2 plasma surface treatment between 2 layers.

Microfabrication of PI-SiC-Mg-SiC-PI Disks for Side Permeation: The 1 µm PI layer was coated on the cleaned and treated glass wafer, then 135 nm PECVD SiC (10 min of deposition) was deposited on the bottom PI. After patterning Ti-Mg-Ti metal stacks, the other 135 nm PECVD SiC was grown on top, and 1 µm PI layer was spin-coated following 2 min 200 W O_2 plasma, and VM 652 treatment. Then, the top 400 nm PECVD SiC was deposited, and the whole encapsulation stack was etched to 4 widths: 20, 50, 100, and 150 µm.

Microfabrication of ECoG Devices: For PI-ECoG devices, after 1 µm PI coated on the cleaned 4 in. glass wafer, 20 nm Ti/100 nm Pt/20 nm Ti metallic layers were sputtered and then patterned by Corial etcher. Before the spin-coating of top 1 µm PI, the substrate was treated by O_2 plasma (200 W, 30s) and adhesion promoter VM652. Then 400 nm SiC was deposited on the top and the PI-SiC layers were etched for opening the electrodes and connections. The PI-SiC ECoG devices were fabricated in the same way except 2 SiC layers (thickness 130 nm) were conformably covered the metal tracks.

Accelerated Aging Test: The Mg disks and ECoG samples were soaked in saline solution (Gibco 1X PBS, pH 7.4, 137 mM NaCl, 2.7 mM KCl, and 4.3 mM Na_2HPO) at 57 °C during the whole experiment except during the optical images capture and EIS measurements.

Optical Mg Test: The glass wafer was flipped and placed on a black PMMA substrate to observe Mg corrosion status. A digital microscope (Leica, DVM6) was used to capture images of Mg disks. The automatic stage of the microscope allowed the spatial mapping and self-capture of images. The parameters of the digital microscope were kept constant during the aging test (zoom: 0.982, exposure time: 15.5 ms, gain: 1, CXL light intensity: 50%, white balance base value: 435, 255, 405 for red, green, and blue).

SEM, FIB Milling, and EDX Analysis: SEM images were acquired with a Zeiss GeminiSEM 300 microscope using an annular detector at a beam energy of 3 keV. For nonconductive samples, a 4 nm thick gold metallization layer was sputter-deposited with a Quorum Q300T Sputter Coater. The cross-sections of the PI-Mg-PI were obtained by FIB milling in a dual beam equipment (Zeiss CrossBeam 540) equipped with Oxford Inst. EDX detector. The current injected for the first rough milling was 7 nA, whereas a finer polishing step at 1.5 nA was performed to clean the cross-section from debris. EDX analysis was performed (with 2 pA current and energy range of 20 keV) on the FIB-milled cross sections.

WVTR Measurement by the Permeation Cell: The WVTR of a 5 µm thick PI film was measured at 47 °C and 85% RH (relative humidity) using a permeation cell (Systech Instrument 7001) with a detection limit of 2×10^{-2} g m^{-2} day^{-1}. The result is shown in Table S1 (Supporting Information).

T-Peel Test: For PI–PI interface adhesion measurement, a 5 µm thick PI layer was spin-coated and baked on a silicon (Si) wafer. Mg rectangles (15 mm length, 8 mm width) were patterned on the PI substrate as the peel arm (Figure S12a, Supporting Information). The top 5 µm thick PI layer was spin-coated and baked with/without pretreatment. For PI–Ti interface, the fabrication was the same of PI–PI samples, except that a 30 nm thick Ti film was sputtered in between 2 layers of 5 µm thick PI. After fabrication, layers were peel from the Si wafer and cut into strips by laser (WS-turret 200, Optec Laser Systems). The width and length of the strips are 8 and 55 mm, including peel arms. Then, the PI samples were loaded on the tensile machine (MTS Universal Testing Machine, MTS Systems) for the peel test. The velocity rate was set as 1 mm s^{-1}.

EIS Measurement: The 9-channel FPCB (flexible printed circuit board, PCBWay) was connected to the ECoG for the EIS measurement. Soldering paste (Sn/Bi/Ag, Chipquik, catalog no. SMDLTLFP10T5) was screen

printed on the interconnect pads and a flexible PCB with matching pads was placed on top. Then the sample was heated at 180 °C for 2 min to solidify the soldering paste. After cooling down, the epoxy (Loctite EA 3430) was drop-casted on the soldering sites and cured at room temperature for 12 h. After fabrication, EIS measurements were performed by soaking the devices under test in a beaker containing PBS solution (Gibco PBS, pH 7.4, 1X), together with a large-area platinum wire as counter electrode and an Ag/AgCl reference electrode (Metrohm, El. Ag/AgCl DJ RN SC: KCl). EIS spectra were acquired using an AUTOLAB PGSTAT302N Metrohm potentiostat (100 mV amplitude, 1 Hz–0.1 MHz frequency range).

Supporting Information

Supporting Information is available from the Wiley Online Library or from the author.

Acknowledgements

The authors would like to acknowledge financial support by the Bertarelli Foundation, InnoSuisse (Grant No. 45944.1 IP-ENG), and the Swiss National Science Foundation SNFS (Grant No. 514359). The authors would like to thanked the staff from the Neural Microsystems Platform (NMP) of the Fondation Campus Biotech Geneva (FCBG) and the EPFL Center for MicroNanofrabrication (CMi) for their help with the microfabrication processes, and the staff of EPFL Interdisciplinary Center for Electron Microscopy (CIME) for assistance in samples' preparation. Open Access Funding is supported by the Ecole Polytechnique Fédérale de Lausanne.

Open access funding provided by Ecole Polytechnique Federale de Lausanne.

Conflict of Interest

The authors declare no conflict of interest.

Data Availability Statement

The data that support the findings of this study are available in the Supporting Information of this article.

Keywords

lag time, Mg corrosion, neural interfaces, side permeation, thin-film encapsulation, water transmission rate

Received: October 2, 2023
Revised: December 8, 2023
Published online: March 19, 2024

[1] H. C. Lee, F. Ejserholm, J. Gaire, S. Currlin, J. Schouenborg, L. Wallman, M. Bengtsson, K. Park, K. J. Otto, *J. Neural Eng.* **2017**, *14*, 036026.
[2] P. A. Markov, D. S. Khramova, K. V. Shumikhin, I. R. Nikitina, V. S. Beloserov, E. A. Martinson, S. G. Litvinets, S. V. Popov, *J. Biomed. Mater. Res.* **2019**, *107*, 2088.
[3] E. N. Zhang, J. Clément, A. Alameri, A. Ng, T. E. Kennedy, D. Juncker, *Adv. Mater. Technol.* **2021**, *6*, 2000909.
[4] C. J. Bettinger, M. Ecker, T. D. Yoshida Kozai, G. G. Malliaras, E. Meng, W. Voit, M. R. S. Bull, **2020**, *45*, 655.
[5] M. Mariello, K. Kim, K. Wu, S. P. Lacour, Y. Leterrier, *Adv. Mater.* **2022**, *34*, 2201129.
[6] H. Fang, J. Zhao, K. J. Yu, E. Song, A. B. Farimani, C.-H. Chiang, X. Jin, Y. Xue, D. Xu, W. Du, K. J. Seo, Y. Zhong, Z. Yang, S. M. Won, G. Fang, S. W. Choi, S. Chaudhuri, Y. Huang, M. A. Alam, J. Viventi, N. R. Aluru, J. A. Rogers, *Proc. Natl. Acad. Sci. USA* **2016**, *113*, 11682.
[7] J. Jeong, F. Laiwalla, J. Lee, R. Ritasalo, M. Pudas, L. Larson, V. Leung, A. Nurmikko, *Adv. Funct. Mater.* **2019**, *29*, 1806440.
[8] C. Li, M. Cauwe, L. Mader, D. Schaubroeck, M. Op de Beeck, *Coatings* **2019**, *10*, 19.
[9] K. Kim, M. Van Gompel, K. Wu, G. Schiavone, J. Carron, F. Bourgeois, S. P. Lacour, Y. Leterrier, *Small* **2021**, *17*, 2103039.
[10] K. Y. Lee, H. Moon, B. Kim, Y. N. Kang, J. Jang, H. K. Choe, S. Kim, *Adv. Mater. Interfaces* **2020**, *7*, 2001152.
[11] C. Wei, Y. Wang, W. Pei, X. Han, L. Lin, Z. Liu, G. Ming, R. Chen, P. Wu, X. Yang, L. Zheng, Y. Wang, *Microsyst. Nanoeng.* **2022**, *8*, 50.
[12] G. Balakrishnan, J. Song, C. Mou, C. J. Bettinger, *Adv. Mater.* **2022**, *34*, 2106787.
[13] J. E. Chung, H. R. Joo, J. L. Fan, D. F. Liu, A. H. Barnett, S. Chen, C. Geaghan-Breiner, M. P. Karlsson, M. Karlsson, K. Y. Lee, H. Liang, J. F. Magland, J. A. Pebbles, A. C. Tooker, L. F. Greengard, V. M. Tolosa, L. M. Frank, *Neuron* **2019**, *101*, 21.
[14] T. Kaiju, M. Inoue, M. Hirata, T. Suzuki, *J. Neural Eng.* **2021**, *18*, 036025.
[15] Z. Zhao, H. Zhu, X. Li, L. Sun, F. He, J. E. Chung, D. F. Liu, L. Frank, L. Luan, C. Xie, *Nat. Biomed. Eng.* **2023**, *7*, 520.
[16] P. van de Weijer, H. B. Akkerman, P. C. P. Bouten, P. Panditha, P. J. M. Klaassen, A. Salem, *Org. Electron.* **2018**, *53*, 256.
[17] P. Boldrighini, A. Fauveau, S. Thérias, J. L. Gardette, M. Hidalgo, S. Cros, *Rev. Sci. Instrum.* **2019**, *90*, 014710.
[18] A. K. Singh, W.-F. Chou, X. Jia, C.-Y. Wang, C. Fuentes-Hernandez, B. Kippelen, S. Graham, *J. Vac. Sci. Technol. A* **2020**, *38*, 033203.
[19] M. Mariello, K. Wu, M. von Allmen, M. van Gompel, S. P. Lacour, Y. Leterrier, in *2022 IEEE International Conference on Flexible and Printable Sensors and Systems (FLEPS)*, IEEE, Vienna, Austria, **2022**, p. 1.
[20] M. Esmaily, J. E. Svensson, S. Fajardo, N. Birbilis, G. S. Frankel, S. Virtanen, R. Arrabal, S. Thomas, L. G. Johansson, *Prog. Mater. Sci.* **2017**, *89*, 92.
[21] D. Biswas, A. Nag, S. Ghosh, A. Pal, S. Biswas, S. Banerjee, A. Pal, *J. Global Res. Comput. Sci.* **2011**, *2*, 118.
[22] S. Kirsten, M. Schubert, J. Uhlemann, K.-J. Wolter, in *2014 36th Annual International Conference of the IEEE Engineering in Medicine and Biology Society*, IEEE, Chicago, IL, **2014**, p. 6561.
[23] M. O. De Beeck, R. Verplancke, D. Schaubroeck, D. Cuypers, M. Cauwe, B. Vandecasteele, J. O'Callaghan, D. Braeken, A. Andrei, A. Firrincieli, M. Ballini, A. Kundu, A. Fahmy, E. Patrick, N. Maghari, R. Bashirullah, J. De Baets, in *2017 IEEE Biomedical Circuits and Systems Conference (BioCAS)*, IEEE, Torino, **2017**, p. 1.
[24] X. Sun, J. Bu, W. Liu, H. Niu, S. Qi, G. Tian, D. Wu, *Sci. Eng. Compos. Mater.* **2017**, *24*, 477.
[25] C. A. Kuliasha, J. W. Judy, *Adv. Mater. Technol.* **2021**, *6*, 2100149.
[26] C. A. Diaz-Botia, L. E. Luna, R. M. Neely, M. Chamanzar, C. Carraro, J. M. Carmena, P. N. Sabes, R. Maboudian, M. M. Maharbiz, *J. Neural Eng.* **2017**, *14*, 056006.
[27] X. Lei, S. Kane, S. Cogan, H. Lorach, L. Galambos, P. Huie, K. Mathieson, T. Kamins, J. Harris, D. Palanker, *Silicon Carbide Technology for Advanced Human Healthcare Applications*, Elsevier, Amsterdam, **2022**, p. 99.